MAGNETOHYDRODYNAMICS IN A DOMAIN BOUNDED BY A SPHERICAL SURFACE: A FOURIER–SPECTRAL ELEMENT APPROXIMATION INVOLVING A DIRICHLET TO NEUMANN OPERATOR FOR THE RESOLUTION OF THE EXTERIOR PROBLEM

Alexandre Fournier [*]

[*] Université Joseph-Fourier
Laboratoire de Géophysique interne et Tectonophysique
Geodynamo Team
Maison des Géosciences, BP 53, 38041 Grenoble Cedex 9, FRANCE
e-mail: Alexandre.Fournier@ujf-grenoble.fr

Key words: Magnetohydrodynamics, Fourier–spectral element method, Dirichlet-to-Neumann, Induction, Dynamo, Taylor–Couette flow

Abstract. *We present a Fourier–spectral element approximation of electromagnetic induction (and magnetohydrodynamics) in a domain bounded by a spherical interface. The electromagnetic problem is cast in terms of electromagnetic potentials, the uniqueness of which is enforced by the choice of Coulomb's gauge. A $P_N - P_{N-2}$ approach ensures the solenoidal character of the magnetic vector potential, and an analytical Dirichlet-to-Neumann operator is constructed to solve implicitly for the exterior problem. The validity and convergence of the method is illustrated by examples of increasing complexity: magnetic free decay, kinematic dynamo action, and magnetohydrodynamic Taylor–Couette flow.*

1 INTRODUCTION

In geophysics, recent years have seen the implementation of grid-based numerical methods to model convection/dynamo action in earth's core[1,2,3], or induction in earth's crust and mantle[4]. In the latter case, such an approach is imposed by the three-dimensional heterogeneities of the medium. Regarding core dynamics, the motivation lies essentially in the scalability of such local methods, which is supposedly better than the one of global spectral methods (relying on spherical harmonics $\mathcal{Y}_l^m$), and should therefore allow us to reach more earth-like parameter regimes. Whereas this remains to be seen, such local approaches face two difficulties with respect to $\mathcal{Y}_l^m$-based methods: the first one concerns the imposition of the divergence-free constraint that applies to the magnetic field **B** (or the magnetic vector potential **A**, if used in conjunction with Coulomb's gauge);

$\bar{\Omega}$
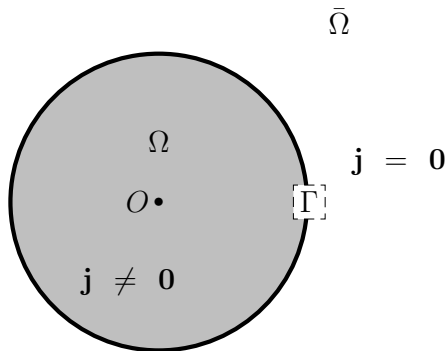
Figure 1: Notations. The computational domain Ω (gray region) contains an electrically conducting fluid, the motion of which can generate electric currents **j**. It is surrounded by an infinite insulating domain $\bar{\Omega}$. These two domains are separated by the surface Γ, which is assumed to be spherical when the analytical Dirichlet to Neumann operator is constructed in section 5.

the second stems from the fact that **B** is defined in $\mathbb{R}^3$. Outside from the region(s) containing its sources (in geophysics, from the top of earth's core up to the ionosphere, say), it must decay in a harmonic fashion. While this translates elegantly into a boundary condition on the surface of the domain in $\mathcal{Y}_l^m$-based methods[5], it is hard to implement in local approaches. Several roads (of increasing complexity) can be followed: one can use approximate boundary conditions[3], or mesh a portion of the source-free region and apply homogeneous Dirichlet boundary conditions at the outermost boundary of this new domain[1,2], or even resort to a boundary element method (BEM) to mimic the presence of the insulating exterior domain[6]. In the context of a Fourier–spectral element discretization of the induction problem in a domain bounded by a spherical surface Γ, we define in this paper a Dirichlet to Neumann operator to apply on Γ that solves implicitly the exterior problem. This approach is less general and elegant than a coupling with a BEM; it is, however, rather straightforward to implement, especially when one wishes to come up with an induction/MHD model starting from a Navier–Stokes solver. Besides, in the framework of a high-order method, its computational cost is limited.

In this paper, emphasis is thus put on the Fourier-spectral element approximation of electromagnetic induction, since the fluid solver we use was already described in a previous paper[7]. Induction is formulated in terms of the electric potential and magnetic vector potential. We recall governing equations, continuity and boundary conditions in section 2, followed by the weak form of this formalism in section 3. After a short description of the Fourier-spectral element method in section 4, the Dirichlet to Neumann operator is extensively described in section 5. The method is then illustrated in section 6 by various numerical examples of increasing complexity (magnetic free decay, kinematic dynamo action, and magnetohydrodynamic spherical Taylor–Couette flow).

2 GOVERNING EQUATIONS AND BOUNDARY/CONTINUITY CONDITIONS

2.1 The induction equation

An electrically conducting fluid is confined in a bounded domain Ω, surrounded by an infinite insulating exterior domain $\bar{\Omega}$ (see Fig. 1). We assume that the fluid of interest has

constant material properties (in particular, its mass density ρ^f and electrical conductivity σ). In what follows, unless otherwise noted, the equations we write apply in Ω.

Induction (and MHD) problems can be cast in terms of the electric (scalar) and magnetic (vector) potentials V and $\mathbf{A}$, respectively[8,9]. These potentials are related the magnetic and electric fields $\mathbf{B}$ and $\mathbf{E}$ by

$$\mathbf{E} = -\boldsymbol{\nabla}V - \partial_t\mathbf{A}, \tag{1}$$
$$\mathbf{B} = \boldsymbol{\nabla}\times\mathbf{A}. \tag{2}$$

As such, the potentials are not unique. Uniqueness is ensured by a gauge condition. We choose Coulomb's gauge[8,9] $\boldsymbol{\nabla}\cdot\mathbf{A} = 0$. In the framework of the magnetohydrodynamic approximation[8,10], induction in Ω is governed by the following set of equations

$$\partial_t\mathbf{A} = -\boldsymbol{\nabla}V + \eta\nabla^2\mathbf{A} + \mathbf{u}\times(\boldsymbol{\nabla}\times\mathbf{A}), \tag{3}$$
$$\boldsymbol{\nabla}\cdot\mathbf{A} = 0, \tag{4}$$

where $\eta = 1/\mu_0\sigma$ is the magnetic diffusivity (μ_0 is the permeability of vacuum). This formulation involves fields whose spatial variations are smoother with respect to the primitive variables $\mathbf{B}$ and $\mathbf{E}$. The current density $\mathbf{j}$ can be retrieved from the knowledge of $\mathbf{A}$ through the equality:

$$\mathbf{j} = (1/\mu_0)\boldsymbol{\nabla}\times\boldsymbol{\nabla}\times\mathbf{A} = -(1/\mu_0)\nabla^2\mathbf{A}. \tag{5}$$

In Eqs. (3)-(4), the electric potential appears as the natural Lagrange multiplier associated with Coulomb's gauge constraint on the magnetic vector potential, and should be solved for. This results in an important computational cost, that one would have to pay anyway if solving directly for $\mathbf{B}$ (through the introduction of a Lagrange multiplier[1,11]). Another interesting feature of this approach, in connection with the exterior problem, is that the normal derivative $\mathbf{A}$ is continuous across Γ (see §2.2).

2.2 Boundary and continuity conditions

2.2.1 General relationships

Let S denote a surface separating two media of different (and finite) electric conductivity σ_- and σ_+, and $\hat{\mathbf{n}}$ be the unit surface vector pointing from medium $-$ to medium $+$, say. We introduce the jump operator $[\ ]$ defined by $[f] = f_+ - f_-$. According to Maxwell's equations and Ohm's law, the following jump conditions hold[12]:

$$[\hat{\mathbf{n}}\times\mathbf{E}] = \mathbf{0}, \ \epsilon_0\,[\hat{\mathbf{n}}\cdot\mathbf{E}] = \chi, \ [\mathbf{B}] = \mathbf{0}, \ [\hat{\mathbf{n}}\cdot\mathbf{j}] = 0,$$

χ being the surface charge density over S. In terms of the potentials $\mathbf{A}$ and V, the previous set of conditions translate into[8]

$$[V] = 0, \tag{6}$$
$$[\mathbf{A}] = \mathbf{0}, \tag{7}$$
$$[\hat{\mathbf{n}}\cdot\boldsymbol{\nabla}\mathbf{A}] = \mathbf{0}, \tag{8}$$

which all apply to the specific case (of interest for us) of a conducting-insulating interface $(\sigma_- = \sigma, \sigma_+ = 0)$. Eq. (8) is particularly useful when deriving the weak formulation associated with the induction problem cast in terms of potentials (see section 3).

2.2.2 Why one should impose $\hat{\mathbf{n}} \cdot \mathbf{A} = 0$ on Γ

With the continuity conditions in mind, let us return to Coulomb's gauge constraint. Taking the divergence of Eq. (5) leads to

$$\boldsymbol{\nabla} \cdot \nabla^2 \mathbf{A} = \nabla^2 \boldsymbol{\nabla} \cdot \mathbf{A} = 0. \tag{9}$$

We need boundary conditions for the gauge to be effectively satisfied. Taking $\hat{\mathbf{n}}\cdot$ Eq. (5) yields

$$-\hat{\mathbf{n}} \cdot \nabla^2 \mathbf{A} = \mu_0 \hat{\mathbf{n}} \cdot \mathbf{j}. \tag{10}$$

Since the normal component of $\mathbf{j}$ is continuous across Γ, we get $\hat{\mathbf{n}} \cdot \nabla^2 \mathbf{A} = 0$. Now, let us write $\hat{\mathbf{n}} \cdot \nabla^2 \mathbf{A}$ as[9]

$$\hat{\mathbf{n}} \cdot \nabla^2 \mathbf{A} = \boldsymbol{\nabla} \cdot (\hat{\mathbf{n}} \times (\boldsymbol{\nabla} \times \mathbf{A})) + \partial_n \boldsymbol{\nabla} \cdot \mathbf{A},$$

which implies

$$\boldsymbol{\nabla} \cdot (\hat{\mathbf{n}} \times (\boldsymbol{\nabla} \times \mathbf{A})) + \partial_n \boldsymbol{\nabla} \cdot \mathbf{A} = 0. \tag{11}$$

What follows is now a restriction to the case of a spherical Γ. With (r, θ, ϕ) the standard spherical coordinates and $(\hat{\mathbf{e}}_r, \hat{\mathbf{e}}_\theta, \hat{\mathbf{e}}_\phi)$ the associated basis, one has

$$\hat{\mathbf{n}} \times (\boldsymbol{\nabla} \times \mathbf{A}) = \frac{1}{r} \left\{ (\partial_\theta A_r - \partial_r(rA_\theta))\hat{\mathbf{e}}_\theta + ((1/\sin\theta)\partial_\phi A_r - \partial_r(rA_\phi))\hat{\mathbf{e}}_\phi \right\}.$$

Let us impose the extra condition

$$A_r = \hat{\mathbf{n}} \cdot \mathbf{A} = 0 \text{ on } \Gamma. \tag{12}$$

$\boldsymbol{\nabla} \cdot \{\hat{\mathbf{n}} \times \boldsymbol{\nabla} \times \mathbf{A}\}$ now writes

$$\boldsymbol{\nabla} \cdot \{\hat{\mathbf{n}} \times \boldsymbol{\nabla} \times \mathbf{A}\} = \frac{1}{r\sin\theta} \left(\partial_\theta \sin\theta(-1/r\partial_r r A_\theta) + \partial_\phi(-1/r\partial_r r A_\phi) \right) \tag{13}$$

The continuity condition (8) implies that both $1/r\partial_r rA_\theta$ and $1/r\partial_r rA_\phi$ are continuous across Γ. If the exterior domain is an insulator, $\mathbf{A}$ is toroidal (see §5.1), and described by a scalar field p such that:

$$\mathbf{A} = \boldsymbol{\nabla} \times (p\boldsymbol{r}) = \frac{1}{\sin\theta}\partial_\phi p\hat{\mathbf{e}}_\theta - \partial_\theta p\hat{\mathbf{e}}_\phi. \tag{14}$$

It is then straightforward to show that the right-hand side of Eq. (13) vanishes. To summarize, if one imposes the boundary condition (12), then $\boldsymbol{\nabla} \cdot \mathbf{A}$ is controlled by

$$\nabla^2 \boldsymbol{\nabla} \cdot \mathbf{A} = 0 \text{ in } \Omega, \tag{15}$$
$$\partial_n \boldsymbol{\nabla} \cdot \mathbf{A} = 0 \text{ on } \Gamma, \tag{16}$$

which means that $\boldsymbol{\nabla} \cdot \mathbf{A}$ is constant. By imposing a zero normal component of $\mathbf{A}$ on Γ, this constant can only be 0.

2.2.3 Boundary condition for the electric potential V

Setting $\hat{\mathbf{n}} \cdot \mathbf{A} = 0$ on Γ imposes, in the case of an insulating exterior domain, the value of the normal derivative of the scalar potential V. Since $\hat{\mathbf{n}} \cdot \mathbf{j} = 0$ on Γ, we have

$$\hat{\mathbf{n}} \cdot \sigma \left(-\partial_t \mathbf{A} - \boldsymbol{\nabla} V + \mathbf{u} \times (\boldsymbol{\nabla} \times \mathbf{A}) \right) = 0 = -\partial_t (\hat{\mathbf{n}} \cdot \mathbf{A}) - \partial_n V + \hat{\mathbf{n}} \cdot (\mathbf{u} \times (\boldsymbol{\nabla} \times \mathbf{A})). \quad (17)$$

The first term vanishes because of Eq. (12), which yields

$$\partial_n V = \hat{\mathbf{n}} \cdot (\mathbf{u} \times (\boldsymbol{\nabla} \times \mathbf{A})) \text{ on } \Gamma. \quad (18)$$

Now, if homogeneous boundary conditions are prescribed for the velocity field $\mathbf{u}$ on Γ (or if there is no flow at all), the electric potential V satisfies a homogeneous Neumann boundary condition:

$$\partial_n V = 0 \text{ on } \Gamma. \quad (19)$$

3 WEAK FORM OF THE $V - \mathbf{A}$ FORMALISM

The similarity of Eqs. (3)–(4) with the Navier–Stokes equations controlling the dynamics of an incompressible fluid suggests to introduce the following functional spaces:

$$L^2 (\Omega) = \left\{ w : \Omega \to \mathbb{R}, \sqrt{\int_\Omega w^2 d\Omega} < +\infty \right\},$$

and

$$\mathbf{H}^1 (\Omega) = \left\{ w_j \in L^2 (\Omega); \ \partial_i w_j \in L^2 (\Omega), i, j = 1, 2, 3, \hat{\mathbf{n}} \cdot \mathbf{w} = 0 \text{ on } \Gamma \right\}.$$

With these spaces at hand, the weak form of the $V - \mathbf{A}$ formalism writes: For all $(\mathbf{w}, \phi) \in \mathbf{H}^1 (\Omega) \times L^2 (\Omega)$, find $(\mathbf{A}, V) \in \mathbf{H}^1 (\Omega) \times L^2 (\Omega)$ such that

$$(\partial_t \mathbf{A}, \mathbf{w}) + (\boldsymbol{\nabla} V, \mathbf{w}) + \eta (\boldsymbol{\nabla} \mathbf{A}, \boldsymbol{\nabla} \mathbf{w}) - \eta (\hat{\mathbf{n}} \cdot \boldsymbol{\nabla} \mathbf{A}, \mathbf{w})_\Gamma - (\mathbf{u} \times (\boldsymbol{\nabla} \times \mathbf{A}), \mathbf{w}) = 0 \quad (20)$$
$$(\boldsymbol{\nabla} \cdot \mathbf{A}, \phi) = 0 \quad (21)$$

in which $(\cdot, \cdot)$ denotes the standard scalar product over the domain Ω, and $(\cdot, \cdot)_\Gamma$ its surface restriction. Integrating by parts the integral involving the electric potential in Eq. (20) leads to

$$\int_\Omega \boldsymbol{\nabla} V \cdot \mathbf{w} d\Omega = \int_\Gamma \hat{\mathbf{n}} \cdot \mathbf{w} V d\Gamma - \int_\Omega V \boldsymbol{\nabla} \cdot \mathbf{w} d\Omega. \quad (22)$$

The test (and shape) functions satisfy the boundary condition (12). We therefore take the first integral on the right hand-side to be zero.

At this stage, the weak form now reads: For all $(\mathbf{w}, \phi)$, find $(\mathbf{A}, V)$ such that

$$(\partial_t \mathbf{A}, \mathbf{w}) - (V, \boldsymbol{\nabla} \cdot \mathbf{w}) + \eta (\boldsymbol{\nabla} \mathbf{A}, \boldsymbol{\nabla} \mathbf{w}) - \eta (\mathcal{K}(\mathbf{A}), \mathbf{w})_\Gamma - (\mathbf{u} \times (\boldsymbol{\nabla} \times \mathbf{A}), \mathbf{w}) = 0 \quad (23)$$
$$(\boldsymbol{\nabla} \cdot \mathbf{A}, \phi) = 0 \quad (24)$$

in which $\mathcal{K}$ denote the Dirichlet to Neumann operator that returns the value of $\hat{\mathbf{n}} \cdot \boldsymbol{\nabla} \mathbf{A}$ on Γ, given $\mathbf{A}$ on Γ. In section 5, we shall provide an explicit formulation for $\mathcal{K}$.
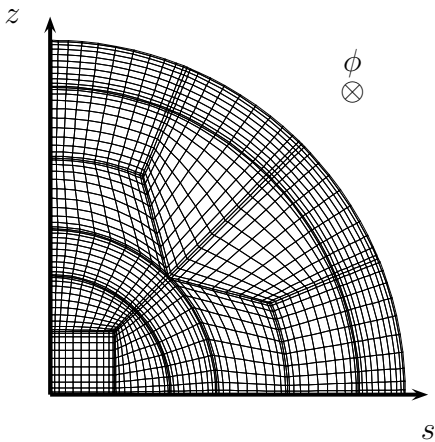
Figure 2: Example of a spectral element mesh used to discretize a semi-meridional cut of the northern hemisphere. Here the polynomial order is set to 11. (s, ϕ, z) are the cylindrical coordinates: cylindrical radius, longitude, and height. Note that a different quadrature is used in the s-direction for those elements sharing an edge with the axis of symmetry.

4 DISCRETIZATION OF THE INDUCTION PROBLEM

The weak formulation (23)–(24) is discretized by means of a Fourier–spectral element method (FSEM) in space, and a second-order semi-implicit scheme in time[7]. Field variables are expanded in Fourier series in the periodic direction (the longitude ϕ), which gives rise to a collection of problems to solve in the semi-meridional plane. These problems are tackled by means of a spectral element method, which is suited to handle the axial singularities that arise when writing the equations in cylindrical coordinates (s, ϕ, z) by resorting to a Gauss–Lobatto–Jacobi (0,1) (GLJ01) quadrature in the direction orthogonal to the axis of symmetry for those elements sharing an edge with that axis. Otherwise, a Gauss–Lobatto–Legendre (GLL) quadrature is used. Spatial discretization is thus characterized by the order of the quadrature (N). An example of a spherical mesh is shown in Fig. 2, for $N = 11$. For a more detailed description of the method, in particular regarding the removal of axial singularities, the reader is referred to Fournier et al.[7].

A $P_N - P_{N-2}$ approach is employed[13] to discretize $\mathbf{A}$ and V, in order to eliminate spurious electric potential modes. The temporal splitting of the resulting coupled problem occurs at the algebraic level[14], resulting in an elliptic problem to solve at each time step to compute the potential correction that will indeed ensure the divergence-free property of $\mathbf{A}$. No boundary conditions are prescribed for the electric potential, and the boundary condition (12) is built in the discrete operators that act upon the vector potential. Diffusive terms are treated fully implicitly, while nonlinear terms are treated explicitly.

The induction problem is therefore very similar to a standard fluid flow problem, with the exception of the treatment of the exterior harmonic problem, which requires to construct a Dirichlet to Neumann (DtN) operator on Γ. The implementation of the DtN operator $\mathcal{K}$ is detailed in the next section.

5 A DIRICHLET TO NEUMANN OPERATOR FOR THE EXTERIOR PROBLEM

In what follows, a denotes the radius of Γ.

5.1 Form of the vector potential in the exterior domain $\bar{\Omega}$

We first recall the analytical form of the solution to the exterior problem, in the source-free region $\bar{\Omega}$. In $\bar{\Omega}$, the magnetic field $\mathbf{B}$ is purely poloidal[8]

$$\mathbf{B} = \boldsymbol{\nabla} \times \boldsymbol{\nabla} \times \boldsymbol{r}p,$$

p being the poloidal scalar; it follows that an appropriate expression for $\mathbf{A}$ is

$$\mathbf{A} = \boldsymbol{\nabla} \times \boldsymbol{r}p + \boldsymbol{\nabla}\psi,$$

in which ψ is a scalar function. The further requirement that $\mathbf{A}$ must follow Coulomb's gauge in $\bar{\Omega}$ implies that ψ satisfies Laplace's equation $\nabla^2\psi = 0$. This, together with the condition that $\mathbf{A}$ must tend to zero getting away from the sources, makes ψ a constant. Therefore, $\mathbf{A}$ can be written as $\mathbf{A} = \boldsymbol{\nabla} \times (\boldsymbol{r}p)$, the spherical components of which are then

$$\mathbf{A} = \frac{1}{\sin\theta}\partial_\phi p \hat{\mathbf{e}}_{\boldsymbol{\theta}} - \partial_\theta p \hat{\mathbf{e}}_{\boldsymbol{\phi}}. \tag{25}$$

In order for the electrical current density $\mathbf{j}$ to be zero (as it should be), $\boldsymbol{\nabla} \times \boldsymbol{\nabla} \times \mathbf{A}$ must vanish everywhere in $\bar{\Omega}$.

$$\mathbf{j} = \boldsymbol{\nabla} \times \boldsymbol{\nabla} \times \mathbf{A} = \frac{1}{\sin\theta}\partial_\phi\left(\frac{\mathcal{L}^2 p}{r^2} - \frac{1}{r}\partial_r^2 rp\right)\hat{\mathbf{e}}_{\boldsymbol{\theta}} + \partial_\theta\left(\frac{1}{r}\partial_r^2 rp - \frac{\mathcal{L}^2 p}{r^2}\right)\hat{\mathbf{e}}_{\boldsymbol{\phi}}, \tag{26}$$

in which $\mathcal{L}^2$ is the Beltrami operator $\mathcal{L}^2 = (-1/\sin\theta)\left(\partial_\theta \sin\theta\partial_\theta + (1/\sin\theta)\partial_\phi^2\right)$. Noticing that the scalar Laplacian writes $1/r\partial_r^2 r - \mathcal{L}^2 T/r^2$ in spherical coordinates, we can enforce the absence of electrical currents by choosing p solution to Laplace's equation $\nabla^2 p = 0$ in $\bar{\Omega}$. Introducing the basis of spherical harmonics $\mathcal{Y}_l^m$ ($\mathcal{Y}_l^m(\theta, \phi) = \bar{P}_l^m(\cos\theta)\exp im\phi$, with $\bar{P}_l^m$ the normalized associated Legendre function of degree l and order m[15]), one can then expand p as

$$p(r \geq a, \theta, \phi, t) = \sum_{l=1}^{l=\infty}\sum_{m=-l}^{m=+l} p_l^m(t)\left(\frac{a}{r}\right)^{l+1}\mathcal{Y}_l^m(\theta, \phi). \tag{27}$$

The coefficients p_l^m can be determined through the knowledge of $\mathbf{A}$ on the boundary Γ (at $r = a$).

5.2 Implementation of the DtN operator

The implementation of the DtN operator proceeds as follows: 1) Given $\mathbf{A}$ on Γ (more precisely its tangential component, since its normal component is zero by construction), compute the p_l^m's. 2) Use Eq. (27) to compute the normal (=radial) derivative of the tangential components of $\mathbf{A}$.

5.2.1 Calculation of the p_l^m's

From Eqs. (25) and (27) (and forgetting about time dependence without loss of generality), we deduce

$$A_\theta(r = a, \theta, \phi) = \frac{1}{\sin\theta} \partial_\phi \sum_{l=1}^{l=\infty} \sum_{m=-l}^{m=+l} p_l^m \mathcal{Y}_l^m(\theta, \phi), \tag{28}$$

$$A_\phi(r = a, \theta, \phi) = -\partial_\theta \sum_{l=1}^{l=\infty} \sum_{m=-l}^{m=+l} p_l^m \mathcal{Y}_l^m(\theta, \phi). \tag{29}$$

In the FSEM approximation of the interior problem, $\mathbf{A}$ is Fourier-decomposed in ϕ

$$\mathbf{A} = \sum_{m=-\infty}^{m=+\infty} \mathbf{A}^m \exp im\phi, \tag{30}$$

and we shall now distinguish between axisymmetric ($m = 0$) and non-axisymmetric ($m \neq 0$) modes.

5.2.2 Axisymmetric mode

By virtue of Eq. (28), we notice that $A_\theta^0(r = a, \theta) = 0$. We also have

$$A_\phi^0 = -\partial_\theta \sum_{l=1}^{l=\infty} p_l^0 \bar{P}_l(\cos\theta). \tag{31}$$

Since $\partial_\theta \bar{P}_l = -\sqrt{l(l+1)}\bar{P}_l^1$, we get the following definition for A_ϕ^0:

$$A_\phi^0 = \sum_{l=1}^{l=\infty} \sqrt{l(l+1)} p_l^0 P_l^1(\cos\theta). \tag{32}$$

If $\langle \cdot, \cdot \rangle$ denotes the scalar product of two functions over a meridian

$$\langle f, g \rangle = \int_{\theta=0}^{\theta=\pi} f(\theta) g(\theta) \sin\theta d\theta, \tag{33}$$

we can write

$$\forall l \in \{1, \ldots, l_{\max}\}, \qquad p_l^0 = \frac{1}{\sqrt{l(l+1)}} \langle A_\phi^0, \bar{P}_l^1 \rangle. \tag{34}$$

Here, $l_{\max}$ denotes the truncation of the spherical harmonic expansion.

5.2.3 Non-axisymmetric modes

Since the colatitudinal component writes

$$A_\theta^m = \frac{im}{\sin\theta} \sum_{l=|m|}^{l\max} p_l^m \bar{P}_l^m(\cos\theta), \tag{35}$$

it is straightforward to get

$$\forall m \neq 0, \qquad p_l^m = \frac{-i}{m} \langle \sin\theta A_\theta^m, \bar{P}_l^m \rangle. \tag{36}$$

5.3 Normal derivative of the magnetic vector potential

With the p_l^ms at hand, the normal derivative of p in $\bar{\Omega}$ can be computed using Eq. (27):

$$\partial_r p(r,\theta,\phi) = \sum_{l=1}^{l\max} \sum_{m=-l}^{m=l} -\frac{l+1}{a} \left(\frac{a}{r}\right)^{l+2} p_l^m \mathcal{Y}_l^m(\theta,\phi). \tag{37}$$

In particular, if $r = a$,

$$\partial_r p(a,\theta,\phi) = \sum_{l=1}^{lmax} \sum_{m=-l}^{m=l} -\frac{l+1}{a} p_l^m \mathcal{Y}_l^m(\theta,\phi). \tag{38}$$

This allows us to write (at last) the normal derivative of $\mathbf{A}$ on Γ :

$$\partial_r A_\theta(r=a,\theta,\phi) = -\frac{1}{\sin\theta}\partial_\phi \sum_{l=1}^{l\max} \frac{l+1}{a} \sum_{m=-l}^{m=l} p_l^m \mathcal{Y}_l^m(\theta,\phi), \tag{39}$$

$$\partial_r A_\phi(r=a,\theta,\phi) = \partial_\theta \sum_{l=1}^{l\max} \frac{l+1}{a} \sum_{m=-l}^{m=l} p_l^m \mathcal{Y}_l^m(\theta,\phi). \tag{40}$$

Thinking again in terms of Fourier modes for the magnetic vector potential, we have

$$\partial_r A_\theta^0 = 0, \tag{41}$$

$$\partial_r A_\theta^m = -\frac{im}{\sin\theta} \sum_{l=|m|}^{l\max} \frac{l+1}{a} p_l^m \bar{P}_l^m(\cos\theta), \text{ for } m \neq 0, \tag{42}$$

$$\partial_r A_\phi^m = \sum_{l=|m|}^{l\max} \frac{l+1}{a} p_l^m \partial_\theta \bar{P}_l^m(\cos\theta), \forall m. \tag{43}$$

Care is needed when evaluating the second of these sums when $\theta = 0$ or π. If $m = \pm 1$, an explicit expression of the $P_l^{\pm 1}$ is necessary in order to remove the apparent singularity. Otherwise, the value of $\partial_r A_\theta^m$ can simply be set to 0.

9

5.4 Computational cost

The evaluation of the normal derivative of $\mathbf{A}$ consists in a round-trip in the spectral world (in colatitude) over Γ. Various quantities involving normalized associated Legendre functions are needed to evaluate the line integrals and subsequent expansions described above – see Eqs. (34), (36), (42), and (43). They are computed initially and stored once and for all at the beginning of a simulation. More precisely, they are evaluated at each one the GLL (or GLJ01) points that belong to Γ. Let us assume that there are N_Γ such collocation points. The number of operations needed to apply the DtN operator is $\mathcal{O}(N_\Gamma l_{\max} m_{\max})$. This has to be compared with the cost of applying the stiffness matrix, which is $\mathcal{O}(n_e N^3 m_{\max})$[7], where n_e is the number of spectral elements and $m_{\max}$ the Fourier truncation in longitude. If $n_{e,\Gamma}$ denotes the number of spectral elements sharing and edge with Γ, N_Γ is approximately $n_{e,\Gamma} N$, and the ratio r of the extra workload due to the DtN operator to the bulk stiffness matrix work is

$$r \approx \frac{n_{e,\Gamma} l_{\max}}{n_e N^2}. \tag{44}$$

Considering the mesh shown in Fig. 2, we find that $r \propto 2.10^{-3} l_{\max}$.

6 NUMERICAL EXAMPLES

6.1 Free decay of fields inside a sphere

We first focus on the free decay of an initially imposed magnetic field, which is governed by a three-dimensional diffusion equation. Our purpose here is to validate the Fourier–spectral element implementation of the DtN operator introduced in section 5, in a simple, linear context, for which an analytical solution exists.

Choosing the radius a of the sphere as the lengthscale and the magnetic diffusion time a^2/η as the timescale, this problem writes: Given $\mathbf{A}_0(\boldsymbol{r}) = \mathbf{A}(\boldsymbol{r}, t = 0)$ and $V_0(\boldsymbol{r}) = V(\boldsymbol{r}, t = 0)$, find $\mathbf{A}(\boldsymbol{r}, t)$ and $V(\boldsymbol{r}, t)$ such that

$$\partial_t \mathbf{A} = \nabla^2 \mathbf{A} - \boldsymbol{\nabla} V \text{ in } \Omega, \tag{45}$$
$$\nabla^2 \mathbf{A} = \mathbf{0} \text{ in } \bar{\Omega}, \tag{46}$$
$$\boldsymbol{\nabla} \cdot \mathbf{A} = 0 \text{ in } \mathbb{R}^3. \tag{47}$$

Taking the divergence of Eq. (45), and using Coulomb's gauge (47) leads to

$$\nabla^2 V = 0 \text{ in } \Omega, \tag{48}$$

which, together with the boundary condition (19), ensures that V is constant in Ω.

6.1.1 Analytical solution

This classical problem can be solved by decomposing the magnetic field into is poloidal (p) and toroidal (q) components – thereby enforcing the divergence free constraint[10].

$$\mathbf{B}(\boldsymbol{r}, t) = \boldsymbol{\nabla} \times \boldsymbol{\nabla} \times \boldsymbol{r} p(\boldsymbol{r}, t) + \boldsymbol{\nabla} \times \boldsymbol{r} q(\boldsymbol{r}, t). \tag{49}$$

The poloidal component of the magnetic field is the only one that survives in an insulating region, and is able to exercise the DtN operator. In the remainder of this example, we thus set $q = 0$ and concentrate on the poloidal case. The scalar field p satisfies a diffusion equation in Ω:

$$\partial_t p = \nabla^2 p, \tag{50}$$

subject to the boundary condition [10]

$$[p] = [\partial_r p] = 0 \text{ on } \Gamma. \tag{51}$$

To find p, we expand it in spherical harmonics $\mathcal{Y}_l^m$

$$p(r, \theta, \phi, t) = \sum_{l=1}^{\infty} \sum_{m=-l}^{l} p_l^m(r, t) \mathcal{Y}_l^m(\theta, \phi). \tag{52}$$

Each degree l and order m is then associated with a one-dimensional radial problem of the form

$$\left[\partial_r^2 + \frac{2}{r} \partial_r - \frac{l(l+1)}{r^2} \right] p_l^m = \partial_t p_l^m, \tag{53}$$

subject to the boundary condition

$$\partial_r p_l^m = -(l+1) p_l^m \text{ on } \Gamma, \tag{54}$$

which ensures that p is harmonic in $\bar{\Omega}$ [10]. The radial dependence is expressed in terms of spherical Bessel functions j_l and we can write

$$p_l^m(r, t) = \sum_{n=1}^{\infty} c_{l,n}^m j_l \left(z_{l-1,n} r \right) \exp(-t / z_{l-1,n}^2). \tag{55}$$

In this expression, $z_{l-1,n}$ is the n-th zero of j_{l-1}. The coefficients $c_{l,n}^m$ can be adjusted so that at $t = 0$ the function (55) takes the required initial value $p_l^m(r, 0)$.

6.1.2 Numerical results

Numerical tests are then defined as follows: pick a (l, m, n) triplet to define the initial poloidal field p_0 as an eigenmode of the diffusion problem, compute the associated initial magnetic vector potential $\mathbf{A}_0 = \boldsymbol{\nabla} \times \boldsymbol{r} p_0$, use this starting field to timestep the problem following the numerical scheme mentioned in §4, measure numerically the associated decay time τ_h, and compare it to the theoretical eigenvalue $\tau_a = z_{l-1,n}^2$. We show results obtained in three instances:

- axial dipole : $(l = 1, m = 0, n = 1)$, hereafter referred to as AD,

- equatorial dipole $(l = 1, m = 1, n = 1)$, hereafter referred to as ED,
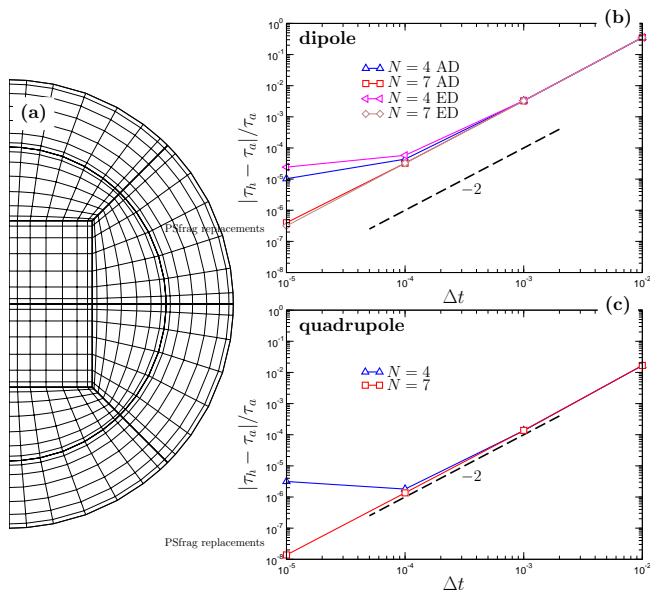
Figure 3: (a): the spectral element mesh used to compute the free magnetic decay times in a sphere, shown here for polynomial order $N = 7$. (b): Relative error in free magnetic decay time as a function of timestep size, for the axial and equatorial dipole AD and ED, respectively, and for polynomial order 4 and 7. The dashed line is indicative of a second order temporal convergence. (c): same as (b) for the equatorial quadrupole EQ.

- equatorial quadrupole ($l = 2, m = 2, n = 1$), hereafter referred to as EQ.

The Bessel functions involved in these cases are[15]

$$j_1(x) = \frac{\sin x}{x^2} - \frac{\cos x}{x} \text{ (AD/ED)}, \tag{56}$$

$$j_2(x) = \left(\frac{3}{x^3} - \frac{1}{x}\right) \sin x - \frac{3}{x^2} \cos x \text{ (EQ)}, \tag{57}$$

and the zeroes needed are $z_{0,1} = \pi$ (AD/ED) and $z_{1,1} = 4.493409$ (EQ) – the latter is numerically determined to machine precision using standard root-finding. Having the azimuthal dependence ranging from $m = 0$ to 2 enables to verify the implementation of the three different types of essential axial conditions to impose on $\mathbf{A}$ within the FSEM framework[7]; more importantly, this also allows us to validate the implementation of the DtN operator, which differs in the axisymmetric ($m = 0$) and non-axisymmetric ($m \neq 0$) cases (§5).

The spectral element grid used to mesh the meridional section of the sphere is represented in Fig. 3a. It consists of $n_e = 10$ spectral elements of polynomial order N ($N = 7$ in Fig. 3a). The truncation level $l_{\max}$ is set to 4, and the timestep Δt spans 3 orders of magnitude, from 10^{-2} down to 10^{-5}, to ensure that there exists a range over which the spatial error dominates, in case spatial convergence is not reached. The latter is studied by setting N to either 4 or 7.

Since they correspond to the same physical situation, results for AD and ED are presented jointly in Fig. 3b, where the relative difference $|\tau_h - \tau_a|/\tau_a$ is shown as a function of the timestep size Δt, on a log-log plot. Results obtained for AD and ED are almost indistinguishable, especially for large timesteps, for which the temporal error dominates.

Decreasing the timestep decreases the error, which becomes eventually dominated by its spatial component in the $N = 4$ case, as the curve flattens for $\Delta t = 10^{-5}$. For $N = 7$, the error keeps on decreasing, which shows that spatial convergence is conclusively reached. Moreover, the slope obtained (-2) confirms the overall order 2 accuracy of the time marching strategy.

Results for the equatorial quadrupole EQ exhibit the same behavior (see Fig. 3c). The agreement between the analytical and numerical solution to this diffusion problem indicates that the DtN operator can be successfully mimic the presence of $\bar{\Omega}$. Note that to obtain this agreement, it is crucial for the spectral element mesh to describe accurately the spherical interface. We do so by resorting to an analytical mapping between the parent element and any curved element touching the interface[16].

6.2 Kinematic dynamo action: The Dudley–James $s2t2$ model

In their comprehensive paper on spherical kinematic dynamos driven by stationary flows, Dudley & James[17] studied in particular the possibility of dynamo action sustained by the following flow

$$\mathbf{u} = \mathcal{U} \left(\boldsymbol{\nabla} \times t_2^0 \hat{\mathbf{e}}_{\boldsymbol{r}} + \epsilon \boldsymbol{\nabla} \times \boldsymbol{\nabla} \times s_2^0 \hat{\mathbf{e}}_{\boldsymbol{r}} \right), \tag{58}$$

in which $\mathcal{U}$ is the velocity scale, t_2^0 and s_2^0 are the toroidal and poloidal scalars, respectively. Here, they are equal, and write

$$s_2^0(r, \theta, \phi) = t_2^0(r, \theta, \phi) = r^2 \sin(\pi r) \bar{P}_2^0(\cos \theta). \tag{59}$$

The flow therefore consists of 2 counter-rotating axisymmetric rolls (its poloidal component ψ_m) carried eastward (westward) in the upper (lower) hemisphere by the zonal wind u_ϕ (its toroidal component) – see Fig. 4. The relative intensity of the rolls with respect to the zonal wind is controlled by the value of ϵ. Using the same scaling as in the previous section, we find that the dimensionless induction equation writes:

$$\partial_t \mathbf{A} = -\boldsymbol{\nabla} V + Rm \mathbf{u} \times (\boldsymbol{\nabla} \times \mathbf{A}) + \nabla^2 \mathbf{A}, \tag{60}$$

in which Rm is the magnetic Reynolds number $Rm = \mathcal{U}a/\eta$. Dudley & James[17] proved numerically the existence of growing magnetic fields sustained by this flow for $\epsilon = 0.14$ and $Rm \gtrsim 54$.

Taking the same value for ϵ, we define the initial magnetic vector potential $\mathbf{A}_0$ as the equatorial dipole seen in §6.1, and monitor the evolution of the induced field to estimate its growth (or decay) rate. For any Rm, after a transient that lasts for a fraction of a magnetic diffusion time, the most unstable (or least stable) induced field mode is the only one remaining, and its evolution obeys an increasing (or decreasing) exponential law. Fig. 4 (right) shows the growth rate versus Rm, for $0 \leq Rm \leq 100$. For $Rm = 0$ (free decay), we retrieve the $-\pi^2$ seen in §6.1. Apart from a small (initial) decrease, we observe a increase of the growth rate with Rm. It eventually becomes positive for

13
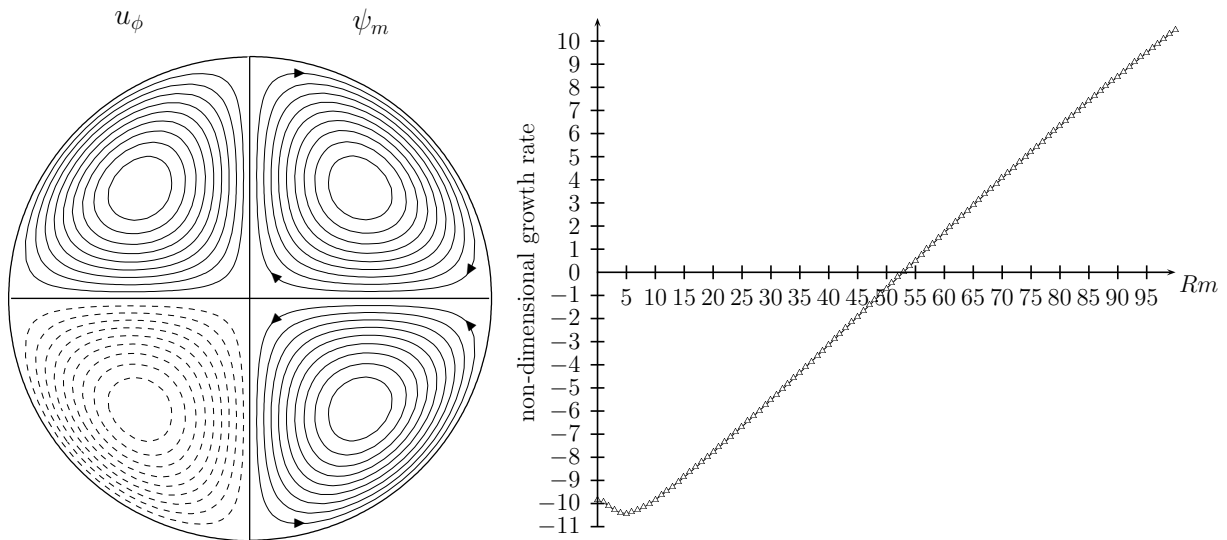
Figure 4: Left: The $s2t2$ flow of Dudley & James[17]. The zonal wind is denoted by u_ϕ and is equatorially-antisymmetric; ψ_m is the meridional stream function, consisting of 2 counter-rotating rolls. The relative amplitude of these two flow components is measured by a dimensionless parameter ϵ. Right: numerical estimate of the growth rate as a function of the magnetic Reynolds number Rm, for $\epsilon = 0.14$. The growth rate is positive for $Rm \gtrsim 53$.

$Rm \gtrsim 53$, in agreement with the estimate of Dudley & James[17]. Using the same mesh as in the free decay case, we find very little sensitivity of the value of the critical magnetic Reynolds number to the spatial resolution (polynomial order N, truncation level $l_{\max}$ for the DtN operator), provided that one sets $N > 7$ and $l_{\max} > 3$. The accuracy is essentially determined by the timestep size Δt, as in the purely diffusive case. With respect to this problem, the novelty here is due to the presence of the electromotive force in the induction equation, which acts potentially as a source of numerical divergence for $\mathbf{A}$, even if the initial $\mathbf{A}$ is divergence-free. In our approximation, the level of $\boldsymbol{\nabla} \cdot \mathbf{A}$ is controlled by the convergence tolerance level δ that one sets when inverting iteratively the elliptic operator acting on the increment of the electric potential (see Fournier et al.[7] for a detailed description of this procedure in the Navier–Stokes case). To illustrate this idea, Fig. 5 (left) shows the timeseries of the quantity

$$\max |\boldsymbol{\nabla} \cdot \mathbf{A}| / \max_{i=s,\phi,z} |A_i|$$

through one magnetic diffusion time, for $Rm = 60$, $\delta = 10^{-6}, 10^{-8}$, and 10^{-10}. The divergence level (as measured by this quantity) appears to be permanently under control as time goes by. Larger values of δ produce the same (scaled) kind of timeseries, but 10^{-6}-10^{-7} is the upper bound to choose if one wants to determine the appropriate growth rate. For completeness, Fig. 5 (right) shows the normal component of the magnetic field $\hat{\mathbf{n}} \cdot \mathbf{B}$ of the eigenmode on Γ. The initial equatorial dipole has been sheared by the zonal wind u_ϕ, and the meridional circulation has generated degree 3 flux patches in the northern
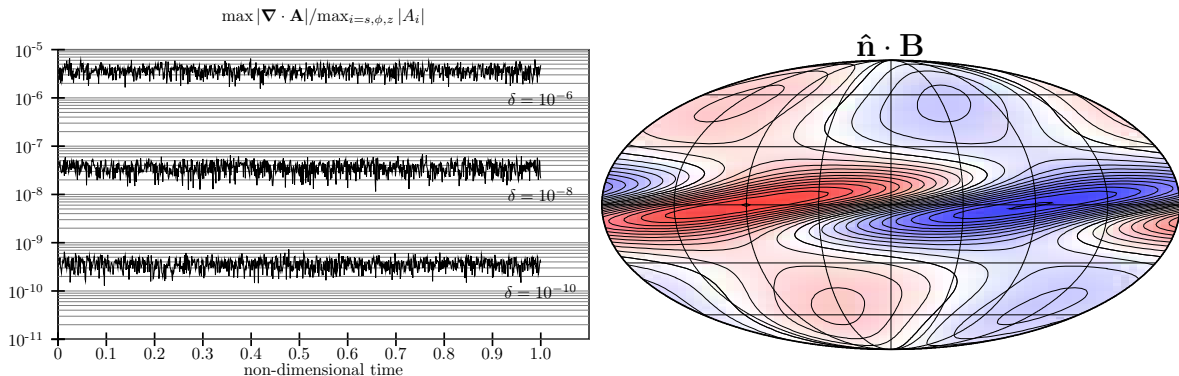
Figure 5: Left: Timeseries of the divergence level, as measured by $\max |\boldsymbol{\nabla} \cdot \mathbf{A}|/\max_{i=s,\phi,z}|A_i|$, for different convergence tolerance level δ in the electric potential solves. Right: the normal component of the magnetic field $\hat{\mathbf{n}} \cdot \mathbf{B}$ on Γ. Scale is arbitrary (kinematic dynamo action); red (resp. blue) indicates positive (resp. negative) values.
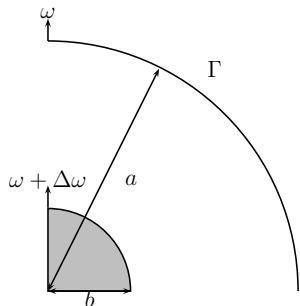
Figure 6: Spherical Taylor–Couette flow set-up. ω and $\omega + \Delta\omega$ are the rotation rates externally imposed to the outer and inner spheres, respectively. The radius ratio γ is defined by $\gamma = b/a$.

and southern hemispheres.

6.3 MHD spherical Taylor–Couette flow

Mechanically-driven liquid metal flows have recently received considerable attention, since they can possibly lead to a self-sustained dynamo regime. This has already been shown experimentally in highly constrained geometries[18,19]. Spherical Taylor–Couette flow is less constrained, and is directly relevant (geometrically speaking) to dynamo action in planetary cores[20](even though dynamo flows in planetary cores are primarily fed by thermo-chemical convection, the vigor of which is hard to reproduce in the laboratory). In Grenoble, the so-called Derviche Tourneur Sodium (DTS) experiment has been built[21]: Sodium is confined between two differentially-rotating spheres, and is permeated by an imposed dipolar magnetic field $\mathbf{B}_0$ (see Nataf et al.[21] for details). This experiments aims at studying the magnetostrophic equilibrium (between the Lorentz and Coriolis forces) and the feasibility (and relevance) of a larger experiment (able to reach higher Rms), that could potentially give rise to a dynamo. Fig. 6 introduces the different notations, and table 1 summarizes the characteristic scales[21]. In non-dimensional form, the set of equations which govern this problem writes, in the frame of reference rotating with the

quantity	scale	symbol
velocity	$b\Delta\omega$	$\mathcal{U}$
length	a	$\mathcal{L}$
time	$\gamma\Delta\omega^{-1}$ with $\gamma = b/a$	
magnetic field	$\|\mathbf{B}_0\|$ at the equator (at the outer sphere)	$\mathcal{B}$
magnetic vector potential	$\mathcal{B}/\mathcal{L}$	
electric potential	$\mathcal{B}/\mathcal{T}$	
pressure	$\mathcal{L}\mathcal{U}\omega$	

Table 1: Scales chosen for the spherical Taylor–Couette problem. The last column on the right indicates the symbols appearing in the definitions of the non-dimensional numbers.

outer sphere,

$$Ro\partial_t\mathbf{u} + Ro(\mathbf{u}\cdot\boldsymbol{\nabla}\mathbf{u}) + 2\hat{\mathbf{e}}_{\boldsymbol{z}}\times\mathbf{u} = -\boldsymbol{\nabla}P + E\nabla^2\mathbf{u} + \frac{EHa^2}{Rm}(\boldsymbol{\nabla}\times\mathbf{B})\times\mathbf{B}, \quad (61)$$

$$\boldsymbol{\nabla}\cdot\mathbf{u} = 0, \quad (62)$$

$$\partial_t\mathbf{A} = -\boldsymbol{\nabla}V + \frac{1}{Rm}\nabla^2\mathbf{A} + \mathbf{u}\times\mathbf{B}, \quad (63)$$

$$\boldsymbol{\nabla}\cdot\mathbf{A} = 0, \quad (64)$$

$$(\mathbf{B} = \boldsymbol{\nabla}\times\mathbf{A}) \quad (65)$$

where

$$Ro = \frac{\mathcal{U}}{\mathcal{L}\omega}, \ E = \frac{\nu}{\omega\mathcal{L}^2}, \ Ha = \frac{\mathcal{B}\mathcal{L}}{\sqrt{\mu_0\rho^f\nu\eta}}$$

are the Rossby, Ekman, and Hartmann numbers, respectively -the definition of Rm has not changed. The kinematic viscosity of the fluid is denoted by ν (all other parameters have appeared before). The ratio of ν to η is the magnetic Prandtl number Pm. For liquid metals, Pm is very small ($Pm \lesssim 10^{-5}$).

The numerical modeling of such flow has received considerable attention over the past few years[22,23,24]; in particular, it has been shown that under certain circumstances, the topology of the induced currents could lead (via the Lorentz force) to fluid regions having an angular velocity larger the one of the inner sphere (the so-called super-rotation)[23,24].

Here we present and discuss briefly preliminary results obtained for this problem, relying on previous studies to assess their validity (in a qualitative sense). These results are obtained for a large value of $Pm(= 1)$, a mild forcing ($Rm = 1$), and a radius ratio $\gamma = 1/3$. The fluid is initially at rest, with both spheres co-rotating at a rate ω ; at $t = 0$ the inner sphere is impulsively set to rotate at $\omega + \Delta\omega$, and our MHD code is timestepped forward in time. The fluid equations are solved in the region comprised between the two spheres, whereas the magnetic equations are solved inside the fluid region and the inner
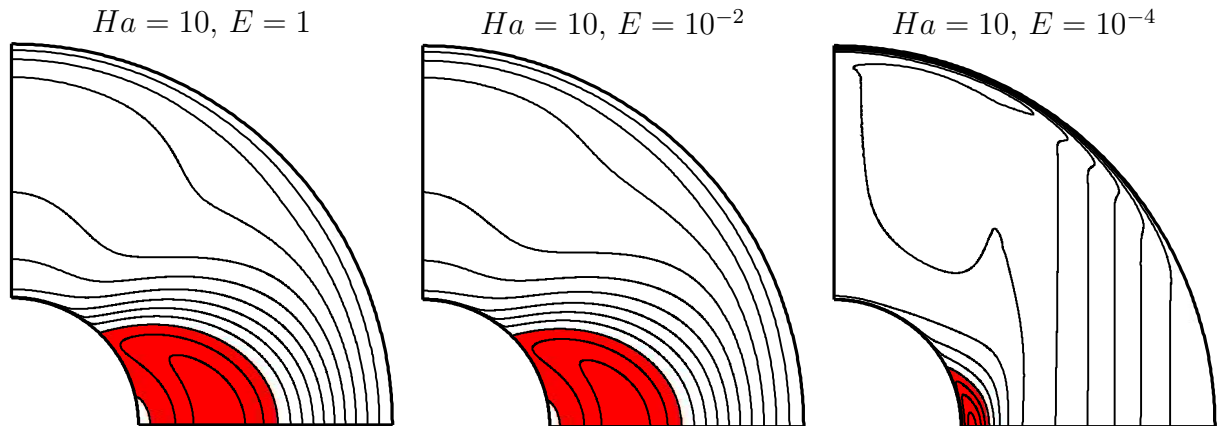
Figure 7: MHD spherical Taylor–Couette flow: maps of the normalized angular velocity $u_\phi/s\Delta\omega$ in the semi-meridional plane. The strength of the imposed magnetic field is constant ($Ha = 10$), as is the level of differential rotation ($Rm = 1$). The background rotation rate increases from left to right by four orders of magnitude ($E = 1$ down to $E = 10^{-4}$). Contours are separated by 1/10, and red indicates super-rotation ($u_\phi/s\Delta\omega > 1$).

sphere. The inner sphere is assumed for simplicity to have the same electrical conductivity as the surrounding fluid. Induced currents can flow inside the sphere, leading to an efficient magnetic coupling between the sphere and the liquid metal in its vicinity[23]. On the outer boundary, the DtN operator is used to mimic the decay of the induced field outside the computational domain. At this moderate forcing, we always find steady, axisymmetric ($m = 0$) solutions. We impose the strength of the imposed magnetic field (setting $Ha = 10$), and study the effect of the background rotation rate ω by varying the Ekman number. In Fig. 7, the normalized angular velocity $u_\phi/s\Delta\omega$ is represented in the northern hemisphere (the solution are equatorially symmetric as well), for $E = 1$, 10^{-2}, and 10^{-4} (from left to right). The imposed field is strong enough to allow for super-rotation (regions of super-rotation are shown in red). For $E = 1$ and 10^{-2} the super-rotating region follows the geometry of the imposed field. For $E = 10^{-4}$, rapid rotation tends to make the flow invariant along the axis of rotation, following the Taylor–Proudman theorem. This is particularly true in those regions near the outer sphere where the imposed field (which decreases like $1/r^3$) is weak. Sufficiently close to the inner sphere, the field is strong enough to overcome this taylorisation, and a tiny region of super-rotation still exists. As can be seen from the momentum equation (61), the pertinent number to quantify the taylorisation of this MHD flow is the Elsasser number $\Lambda = EHa^2/Rm = \mathcal{B}^2/\mu_0\mathcal{L}\omega\mathcal{U}$. As Ha is defined by the value of $\|\mathbf{B}_0\|$ on the outer sphere Γ, $\Lambda > 1$ implies that magnetic effects dominate throughout Ω. This is the case for $E = 1$ ($\Lambda = 10^2$) and $E = 10^{-2}$ ($\Lambda = 1$). For $\Lambda < 1$, the outermost regions of the fluid are dominated by the effects of rotation, as is the case for $E = 10^{-4}$ ($\Lambda = 10^{-2}$).

Albeit encouraging, these preliminary results correspond to parameters far away from the experimental ones[21]. Before pushing them into unknown territories, a benchmark
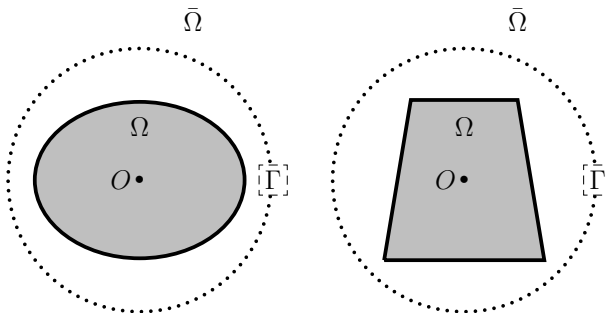
Figure 8: Sketch illustrating the possible extension of the approach detailed in this paper to elliptical (left) and trapezoidal (right) geometries.

with other, $\mathcal{Y}_l^m$-based, codes[23,25,26] needs to be performed. Such a benchmark is currently being set up[27], and will allow us to get a quantitative feeling of the accuracy and relevance of our approach.

7 CONCLUSION

In the context of the numerical approximation of electromagnetic induction or magnetohydrodynamics inside a bounded domain Ω, we have presented a solve strategy relying on a $(V, \mathbf{A})$ potential formulation, discretized with a Fourier–spectral element method (FSEM). It includes a Dirichlet to Neumann operator that corrects the boundary values of $\mathbf{A}$ to account for its harmonic decay in the exterior domain $\bar{\Omega}$. The cost of this operator is reasonable for a high-order method such as the FSEM. This approach could be extended to a non-spherical Ω, provided that one meshes a buffer region between Ω and an imaginary spherical interface Γ that contains Ω (see Fig. 8). Magnetic diffusion should be solved within this buffer region, and the DtN operator used to correct for the value of the diffusing field on Γ.

Even if further tests are needed to assess the efficiency and accuracy of this method, preliminary tests show good agreement with reference solutions and suggest that this approach could provide a good compromise between local (grid-based) and global (spectral) numerical models of planetary core dynamics.

References

1. K. H. Chan, K. Zhang, J. Zou, and G. Schubert. A non-linear, 3-D spherical α^2 dynamo using a finite element method. *Phys. Earth Planet. Inter.*, 128:35–50, 2001.

2. H. Matsui and H. Okuda. MHD dynamo simulation using the GeoFEM platform–verification by the dynamo benchmark test. *Int. J. Comp. Fluid Mech.*, 19:15–22, January 2005.

3. H. Harder and U. Hansen. A finite-volume solution method for thermal convection and dynamo problems in spherical shells. *Geophys. J. Int.*, 161:522–532, May 2005.

4. M. Everett and A. Schultz. Geomagnetic induction in a heterogenous sphere: Azimuthally symmetric test computations and the response of an undulating 660-km discontinuity. *J. Geophys. Res.*, 101(B02):2765–2783, 1996.

5. G. A. Glatzmaier. Numerical simulations of stellar convective dynamos I. The model and method. *J. Comput. Phys.*, 55:461–484, 1984.

6. A. B. Iskakov, S. Descombes, and E. Dormy. An integro-differential formulation for magnetic induction in bounded domains: boundary element-finite volume method. *J. Comput. Phys.*, 197:540–554, July 2004.

7. A. Fournier, H.-P. Bunge, R. Hollerbach, and J.-P. Vilotte. A Fourier-spectral element algorithm for thermal convection in rotating axisymmetric containers. *J. Comput. Phys.*, 204:462–489, 2005.

8. H. K. Moffatt. *Magnetic Field Generation in Electrically Conducting Fluids.* Cambridge Univ. Press, 1978.

9. O. Bíró and K. Preis. On the use of the magnetic vector potential in the finite element analysis of three-dimensional eddy currents. *IEEE Trans. Magn.*, 25:3145–3159, 1989.

10. G. E. Backus, R. Parker, and C. Constable. *An Introduction to Geomagnetism.* Cambridge Univ. Press, 1996.

11. N. Ben Salah, A. Soulaïmani, and W.G. Habashi. A finite element method for magnetohydrodynamics. *Comp. Meth. Appl. Mech. & Engng.*, 190:5867–5892, 2001.

12. P. H. Roberts. *An Introduction to Magnetohydrodynamics.* Longmans, London, 1967.

13. C. Bernardi, M. Dauge, and Y. Maday. *Spectral Methods for Axisymmetric Domains*, volume 3 of *Series in Applied Mathematics.* Gauthier-Villars, Paris, 1999. Numerical algorithms and tests due to Mejdi Azaïez.

14. P. F. Fischer. An overlapping Schwarz method for spectral element solution of the incompressible Navier–Stokes equations. *J. Comput. Phys.*, 133:84–101, 1997.

15. G. B. Arfken and H. J. Weber. *Mathematical Methods for Physicists.* Academic Press, 4 edition, 1995.

16. A. Fournier, H.-P. Bunge, R. Hollerbach, and J.-P. Vilotte. Application of the spectral element method to the axisymmetric Navier-Stokes equation. *Geophys. J. Int.*, 156:682–700, 2004.

17. M.L. Dudley and W.R. James. Time-dependent kinematic dynamos with stationary flows. *Proc. R. Soc. Lond. A*, 425:407–429, 1989.

18. A. Gailitis, O. Lielausis, E. Platacis, S. Dement'ev, A. Cifersons, G. Gerbeth, T. Gundrum, F. Stefani, M. Christen, and G. Will. Magnetic Field Saturation in the Riga Dynamo Experiment. *Phys. Rev. Lett.*, 86:3024–3027, April 2001.

19. R. Stieglitz and U. Müller. Experimental demonstration of a homogeneous two-scale dynamo. *Phys. Fluids*, 13:561–564, 2001.

20. P. Cardin, D. Brito, D. Jault, H.-C. Nataf, and J.-P. Masson. Towards a rapidly rotating liquid sodium dynamo experiment. *Magnetohydrodynamics*, 38:177–189, 2002.

21. H.-C. Nataf, T. Alboussière, D. Brito, P. Cardin, N. Gagnière, D. Jault, J.-P. Masson, and D. Schmitt. Experimental study of super-rotation in a magnetostrophic spherical Couette flow. *Geophys. Astro. Fluid Dyn.*, in press.

22. R. Hollerbach. Magnetohydrodynamic Ekman and Stewartson layers in a rotating spherical shell. *Proc. R. Soc. Lond. A*, 444:333–346, 1994.

23. E. Dormy, P. Cardin, and D. Jault. MHD flow in a slightly differentially rotating spherical shell, with conducting inner core, in a dipolar magnetic field. *Earth Planet. Sci. Lett.*, 160:15–30, 1998.

24. R. Hollerbach. Magnetohydrodynamic flows in spherical shells. In C. Egbers and G. Pfister, editors, *Physics of rotating fluids*, volume 549 of *Lecture notes in Physics*, pages 295–316. Springer, 2000.

25. R. Hollerbach. A spectral solution of the magneto-convection equations in spherical geometry. *Int. J. Numer. Meth. Fluids*, 32:773–797, 2000.

26. E. Dormy, D. Jault, and A. M. Soward. A super-rotating shear layer in magnetohydrodynamic spherical Couette flow. *J. Fluid. Mech.*, 452:263–291, 2002.

27. P. Cardin. Personal communication.